AIMS Mathematics, 10(11): 27985–28003.
DOI: 10.3934/math.20251229
Received: 22 July 2025
Revised: 18 November 2025
Accepted: 26 November 2025
Published: 28 November 2025

https://www.aimspress.com/journal/Math

Research article

Multifractal time series analysis of grounding resistance in transmission line towers under cold-climate conditions

Guangxin Zhang[1], **Minzhen Wang**[1], **Jian Wang**[2] **and Junseok Kim**[3,*]

[1] College of Science and Technology, Ningbo University, Ningbo, 315300, China
[2] School of Mathematics and Statistics, Nanjing University of Information Science and Technology, Nanjing, 210044, China
[3] Department of Mathematics, Korea University, Seoul, 02841, Republic of Korea

* **Correspondence:** Email: cfdkim@korea.ac.kr.

Abstract: In this paper, we investigated the influence of climatic factors, particularly low temperature and humidity, on the grounding resistance of transmission towers in severely cold regions. Drawing on a full year of field monitoring data, we first identified a clear negative linear correlation between temperature and grounding resistance. Notably, the inclusion of precipitation as an additional variable led to a significant increase in the model's explanatory power and indicated that the resistance behavior was influenced by multiple environmental factors. To further explore the nonlinear and dynamic aspects of this relationship, we used multifractal detrended fluctuation analysis (MF-DFA) and multifractal detrended cross-correlation analysis (MF-DCCA). The computational results showed that the resistance time series exhibits strong multifractal characteristics and suggests high variability across temporal scales. Moreover, the combined influence of temperature and precipitation demonstrated a markedly stronger cross-correlation with resistance than temperature alone. These findings emphasize the complex and multiscale nature of grounding behavior in harsh climates and underscore the importance of moving beyond simplified linear models. Our research offers both methodological insights and practical implications for the design, maintenance, and risk assessment of power transmission infrastructure operating under extreme weather conditions, particularly in high-latitude or alpine environments.

Keywords: multifractal analysis; MF-DFA; MF-DCCA; grounding resistance; time series
Mathematics Subject Classification: 37M10, 62M10

1. Introduction

The function of the grounding resistance of overhead transmission line towers is to guide the impulse current or lightning current into the ground through the natural grounding and artificial horizontal grounding body of the tower foundation under lightning strike state, to protect the safety of equipment. The grounding of transmission towers is the most important part of transmission lines and is one of the indispensable measures to prevent lightning disasters. To ensure the safe and stable operation of the transmission system, it is particularly important to observe the grounding resistance of transmission towers, especially to explore the factors that affect the grounding resistance value.

The design of grounding systems is fundamentally dependent on soil properties, with soil resistivity being a core parameter [1]. It is widely established that soil resistivity is not static but is intricately influenced by a multitude of meteorological factors, such as soil humidity, temperature, and precipitation [2, 3]. Early research established foundational models for this relationship; for instance, Soares Gerscovich and Vipulanandan [4] proposed a hyperbolic model, while Bhatt and Jain [5] explored the nonlinear regression between soil moisture and resistivity. Subsequent studies consistently demonstrated that grounding resistance exhibits significant seasonal variations [6, 7], with researchers like Coelho et al. [8] highlighting the combined effects of surface soil, deeper resistivity, and grounding system topology. To handle these complex relationships, methods like Artificial Neural Networks (ANN) has been used to estimate resistance values from meteorological data [9]. Building on this, researchers have delved into advanced modeling and specific environmental challenges. For example, Rani et al. [10] utilized machine learning to evaluate the impact of soil moisture, AL-Mahemmdi et al. [11] assessed the effects of seasonal variations on grounding resistance, and Yuan et al. [12] studied the significant impact of freeze-thaw cycles in cold regions.

Although these models provide valuable insights, they often simplify the complex, dynamic, and nonlinear interactions inherent in the soil-climate system. Conventional linear correlation methods, in particular, may not adequately capture the underlying multiscale dynamics. To address this gap, we adopt multifractal detrended fluctuation analysis (MF-DFA) [13, 14] and multifractal detrended cross-correlation analysis (MF-DCCA) [15]. These algorithms are powerful tools for identifying multifractal properties and scaling behaviors in nonstationary time series, making them well-suited for exploring the coupled, nonlinear relationships among temperature, humidity, and grounding resistance. The applicability of these methods is supported by their successful use across scientific domains, including finance [16, 17], meteorology [18], and geophysics [19]. Geophysical researchers, for example, have used MF-DFA to characterize seismic sequences [20] and MF-DCCA to analyze cross-correlations between land surface temperature and precipitation [21], while others have applied them to soil temperature and humidity time series [22]. Wang et al. [23] proposed a hybrid MRI classification model that combines MF-DFA and the Allen–Cahn equation [24] to improve classification accuracy. Wang et al. [25] presented a one-dimensional multifractal local fitting DFA method using traditional MF-DFA. These applications demonstrate the robust potential of MF-DFA/DCCA for uncovering complex nonlinear dynamics. However, we also acknowledge the potential limitations of MF-DCCA [26], which may induce spurious correlations under certain conditions. Informed by the work of Oswiecimka et al. [27], we give special attention to these potential biases in the experimental analysis and conducted robustness analysis to ensure the robustness and validity of the research results.

Furthermore, we endeavor to connect its data-driven, model-free analysis to the broader literature

on adaptive and stability-guaranteed learning for systems with unknown dynamics. In the absence of a complete physical model, learning from data to ensure system stability is a frontier issue. For instance, Meng et al. [28] proposed a model-free robust optimal control algorithm based on Adaptive Dynamic Programming. In a similar vein, methods like Neural Ordinary Differential Equations [29] offer tools for learning system dynamics, while frameworks such as Control Barrier Functions [30] provide rigorous stability guarantees. Accordingly, the multifractal characteristics and cross-correlations identified in this study offer a quantitative basis for the future design and validation of such adaptive models for grounding system performance.

In this study, we aim to move beyond simple linear correlations by using multifractal analysis to quantify the complex, non-linear dynamics and long-range cross-correlations between meteorological factors and grounding resistance. The application of this method is theoretically justified because grounding resistance emerges from a complex climate-soil system, where multifractal meteorological inputs interact with heterogeneous soil properties and non-linear processes, and this interaction inherently produces a signal that possesses multifractal characteristics.

The outline of this article is shown as follows. In Section 2, we introduce two methods, MF-DFA and MF-DCCA. In Section 3, we give the data sources used for the numerical experiments. In Section 4, we investigate the correlations between the grounding resistance and the meteorological factors according to the time series data. Conclusions are given in Section 5.

2. Methodology

2.1. MF-DFA

Multifractal Detrended Fluctuation Analysis (MF-DFA) is an advanced methodology for studying the multifractal properties of signals and time series. This tool is crucial in many scientific fields for understanding the multifractal nature of data. The MF-DFA algorithm unfolds through five sequential steps:

(1) Construction of the integrated profile: Given a time series $x(i)$ for $i = 1, 2, \ldots, N$, with N being the length, $Y(i)$ is constructed as follows:

$$Y(i) = \sum_{k=1}^{i} \{x(k) - \overline{x}\}, \quad i = 1, 2, \ldots, N. \tag{2.1}$$

Here, $x(k)$ is the k-th value of the original time series, $\overline{x}$ is the mean of the series, and $Y(i)$ is the resulting cumulative sum profile.

(2) Segmentation and detrending: The profile $Y(i)$ is segmented into $M_s \equiv \text{int}(N/s)$ non-overlapping segments of equal length s. This process is also applied from the series end, resulting in $2M_s$ segments. In each segment v, the local trend is determined and removed. This is achieved by fitting a polynomial function to the data in the segment using a least-squares fit, a standard method that minimizes the sum of squared differences between the profile and the fitting polynomial. We use a polynomial of order m, denoted $p_v^m(i)$, to represent this local trend.

(3) Calculation of the fluctuation function: The fluctuation function for each segment v is calculated by the variance between the integrated profile and its local trend. This is performed for segments from both the beginning and the end of the series. For segments from the

beginning ($v = 1, 2, \ldots, M_s$):

$$F^2(s, v) = \frac{1}{s} \sum_{i=1}^{s} \left[Y((v-1)s + i) - p_v^m(i) \right]^2, \tag{2.2}$$

for segments from the end ($v = M_s + 1, M_s + 2, \ldots, 2M_s$):

$$F^2(s, v) = \frac{1}{s} \sum_{i=1}^{s} \left[Y(N - (v - M_s)s + i) - p_v^m(i) \right]^2, \tag{2.3}$$

where $F^2(s, v)$ represents the variance of the detrended profile within the v-th segment of size s.

The q-th order fluctuation function $F_q(s)$ is then obtained by averaging over all segments, for q real, including negative and positive values, as follows:

$$F_q(s) = \left[\frac{1}{2M_s} \sum_{v=1}^{2M_s} \left(F^2(s, v) \right)^{\frac{q}{2}} \right]^{\frac{1}{q}}, \tag{2.4}$$

where $F_q(s)$ is the q-th order overall fluctuation function for a given scale s, and q is the moment order, which can be any real number except zero. However, for $q = 0$, which cannot be directly computed due to division by zero, we use a logarithmic averaging:

$$F_0(s) = \exp \left[\frac{1}{2M_s} \sum_{v=1}^{2M_s} \ln \left(F^2(s, v) \right) \right]. \tag{2.5}$$

(4) Multifractal scaling analysis and spectrum determination: The q-th order fluctuation function $F_q(s)$ is expected to follow a power-law relationship with the scale s, such that $F_q(s) \propto s^{H(q)}$. The exponent $H(q)$ is known as the generalized Hurst exponent. The behavior of $H(q)$ across values of q reveals the fractal nature of the time series. If $H(q)$ is constant for all q, the series is monofractal; if $H(q)$ depends on q, the series is multifractal. The value of the generalized Hurst exponent indicates the nature of the temporal correlations in the series. For $q = 2$, which corresponds to the classical Hurst exponent:

- $H(2) > 0.5$ indicates persistent or long-range positive correlations, where an increase is likely to be followed by another increase, and a decrease by a decrease.
- $H(2) < 0.5$ indicates anti-persistent or long-range negative correlations, where an increase is likely to be followed by a decrease, and vice versa.
- $H(2) = 0.5$ suggests a lack of long-range correlations, characteristic of a random walk process.

The multifractality degree is quantifiable through the range of Hurst exponents, $\Delta H = H(q_{\max}) - H(q_{\min})$. The multifractal spectrum $f(\alpha)$ is derived from the scaling exponent $\tau(q) = qH(q) - 1$ through a Legendre transform: $\alpha = d\tau(q)/dq$ and $f(\alpha) = q\alpha - \tau(q)$. In this transform, $\tau(q)$ is the multifractal scaling exponent, α is the singularity strength, and $f(\alpha)$ is the multifractal spectrum, which represents the fractal dimension of the subset of the series characterized by the singularity strength α. The width of this spectrum, defined as $\Delta\alpha = \alpha_{\max} - \alpha_{\min}$ (where $\alpha_{\max}$ and $\alpha_{\min}$ are the maximum and minimum values of α for which $f(\alpha) > 0$) serves as a key indicator of the degree of multifractality. A broader spectrum (a larger $\Delta\alpha$) signals stronger multifractality.

In this paper, MF-DFA is performed using a second order polynomial detrending ($m = 2$) to capture local nonlinear structure in the integrated profiles. The scale range is set to $s \in [20, 30]$ with 11 discrete scales to balance statistical stability and temporal resolution. The q-th order fluctuation functions are computed over a symmetric range $q \in [-10, 10]$ with 21 equally spaced moments. The case $q = 0$ is treated via logarithmic averaging. Generalized Hurst exponents $H(q)$ are estimated by linear least squares regression of $\log F_q(s)$ versus $\log s$, followed by the computation of scaling exponents $\tau(q) = qH(q) - 1$, the singularity spectrum $(\alpha, f(\alpha))$, and the multifractal spectrum width $\Delta\alpha$, which quantifies the degree of multifractality.

2.2. MF-DCCA

The MF-DCCA emerges as a robust extension designed to scrutinize the multifaceted interrelations between pairs of non-stationary time series.

Herein, we delineate the core steps integral to the MF-DCCA process:

(1) Preparation of cumulative sequences: Starting with two distinct time series X_j and Y_j, where $j = 1, 2, \ldots, N$. Calculate their respective means, $\overline{X}$ and $\overline{Y}$, as $\overline{X} = \frac{1}{N}\sum_{j=1}^{N} X_j$ and $\overline{Y} = \frac{1}{N}\sum_{j=1}^{N} Y_j$. Thereafter, construct the cumulative sequences ($P(j)$ and $R(j)$) from these series:

$$P(j) = \sum_{m=1}^{j}(X_m - \overline{X}), \quad j = 1, 2, \ldots, N, \tag{2.6}$$

$$R(j) = \sum_{m=1}^{j}(Y_m - \overline{Y}), \quad j = 1, 2, \ldots, N. \tag{2.7}$$

(2) Segmentation into scales: Divide the integrated sequences $P(j)$ and $R(j)$ into segments of equal length s, yielding a total of $2N_s$ segments for each series, with $N_s = \text{int}\left(\frac{N}{s}\right)$.

(3) Polynomial fitting: Similar to the procedure in MF-DFA, a polynomial of degree k is fitted to each segment using the least-squares method to determine the local trends, producing $\hat{P}_v(i)$ and $\hat{R}_v(i)$:

$$\hat{P}_v(i) = a_0 + a_1 i + a_2 i^2 + \ldots + a_k i^k, \quad i = 1, 2, \ldots, s, \tag{2.8}$$

$$\hat{R}_v(i) = b_0 + b_1 i + b_2 i^2 + \ldots + b_k i^k, \quad i = 1, 2, \ldots, s, \tag{2.9}$$

where $\hat{P}_v(i)$ and $\hat{R}_v(i)$ are the polynomial fits of degree k for the v-th segment of the profiles P and R, respectively. The coefficients $a_0, \ldots, a_k$ and $b_0, \ldots, b_k$ are determined by a least-squares fit.

(4) Covariance computation: Calculate the detrended covariance for each segment to quantify the degree of cross-correlation:

$$F^2(s, v) = \frac{1}{s}\sum_{i=1}^{s}\left|P((v-1)s + i) - \hat{P}_v(i)\right| \cdot \left|R((v-1)s + i) - \hat{R}_v(i)\right|, \quad v = 1, \ldots, N_s, \tag{2.10}$$

$$F^2(s, v) = \frac{1}{s}\sum_{i=1}^{s}\left|P(N - (v - N_s)s + i) - \hat{P}_v(i)\right| \cdot \left|R(N - (v - N_s)s + i) - \hat{R}_v(i)\right|, v = N_s + 1, \ldots, 2N_s. \tag{2.11}$$

(5) Scaling analysis and multifractal spectrum determination: Similarly, the cross-correlation fluctuation function $F_q(s)$ is expected to scale as a power-law with s: $F_q(s) \propto s^{H_{xy}(q)}$, where $H_{xy}(q)$ is the generalized cross-correlation exponent. The interpretation of $H_{xy}(q)$ for $q = 2$ is as follows:

- $H_{xy}(2) > 0.5$ indicates persistent cross-correlations, meaning that fluctuations in the two series tend to change in the same direction.
- $H_{xy}(2) < 0.5$ indicates anti-persistent cross-correlations, meaning that fluctuations in the two series tend to change in opposite directions.
- $H_{xy}(2) = 0.5$ suggests that the two time series are not long-range cross-correlated.

Multifractality in the cross-correlation is evidenced by the variability of $H_{xy}(q)$ with q. The mass exponent $\tau_{xy}(q)$ and the singularity spectrum $f_{xy}(\alpha)$ are calculated analogously to the MF-DFA case. First, the scaling exponent is defined as $\tau_{xy}(q) = qH_{xy}(q) - 1$. Then, the multifractal spectrum is obtained through the Legendre transform: $\alpha = d\tau_{xy}(q)/dq$ and $f(\alpha) = q\alpha - \tau_{xy}(q)$. The width of the singularity spectrum $\Delta\alpha = \alpha_{xy_{\max}} - \alpha_{xy_{\min}}$ quantifies the degree of multifractal cross-correlation.

In this paper, to quantify multifractal cross correlations between resistance and meteorological variables, we use MF-DCCA. Both series are mean centered and cumulatively integrated to form profile functions. Local polynomial detrending of order $k = 2$ is applied within each scale segment to mitigate nonstationary trends. The scale range is set to $s \in [10, 20]$ with 11 discrete scales, balancing robustness and temporal resolution. For each scale, forward and backward segmentation is performed, and detrended covariances are computed. The q-th order fluctuation function is evaluated over $q \in [-10, 10]$ with 21 equally spaced moments; logarithmic averaging is used for $q = 0$. Generalized cross Hurst exponents $H_{xy}(q)$ are estimated by linear regression of $\log F_q(s)$ against $\log s$, followed by the computation of the mass exponent $\tau_{xy}(q) = qH_{xy}(q) - 1$ and the singularity spectrum $(\alpha_{xy}, f_{xy}(\alpha))$. The multifractal spectrum width $\Delta\alpha_{xy}$ is used to quantify cross scale multifractality of Temperature/Resistance and Temperature+precipitation/Resistance pairs.

3. Data collection

To study the correlation between meteorological factors and grounding resistance, we collect real grounding resistance data from a transmission line tower in Jilin Province using a resistance detector and the ETCR2800 Non-contact Grounding Resistance Online Detection Device, which is shown in Figure 1(a). Figure 1(b) shows the environment of the data collection area, and Figure 1(c) shows the resistance detector setup. This device is designed and manufactured for online monitoring of the connection status of grounding conductors, loop grounding resistance, and metal loop bonding resistance. Unlike the traditional "three-point method" measurement, the device uses a non-contact grounding resistance measurement method. The measurement principle is based on electromagnetic induction, where the circular sensor is placed around the grounding electrode, and grounding resistance is measured using the principle of electromagnetic induction, without the need to insert electrodes into the soil.

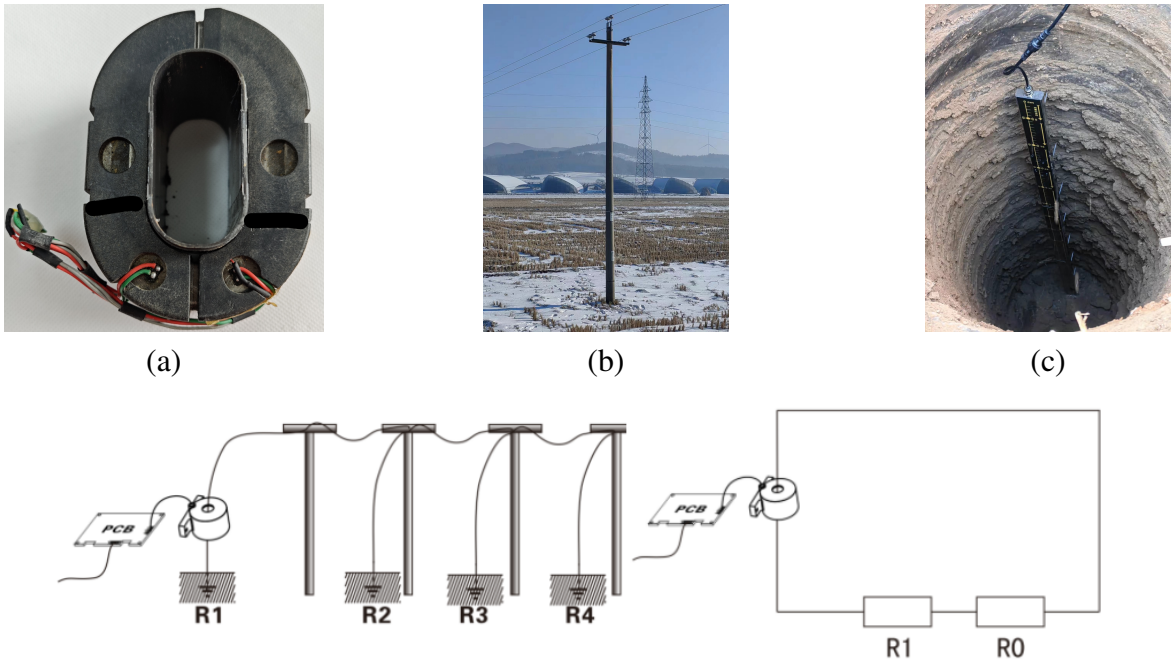

Figure 1. (a) The nature environment of the transmission line tower location, and (b) the access condition of the resistance detector. Time series of precipitation data, and precipitation value (c) used for multiple linear regression. (d) The equivalent circuit diagram of the ground resistance measurement for the transmission tower. We have connected multiple grounding points through the overhead ground wire, forming a multi-point grounding system.

The device consists of a sensor and a circuit board module. The sensor's dimensions are 160×125×90mm, with an aperture of 53×20mm and a weight of approximately 1989g. The maximum operating current of the device is 50mA Max, and it is connected through an overhead grounding conductor to form a multi-point grounding system, making detection very convenient. The device works based on the following principles: The excitation signal is generated by a high-frequency excitation source (typically in the range of 10 to 100kHz) embedded within the sensor. This source generates an alternating magnetic field through the excitation coil. The sensor used in this study uses a square wave signal with a 5V amplitude and a 20kHz frequency to drive the magnetic core, forming a closed magnetic circuit. The grounding conductor cuts the magnetic flux lines within the alternating magnetic field, inducing an electric current (I) according to Faraday's law of electromagnetic induction. The magnitude of this induced current is inversely proportional to the grounding resistance R_L (I = E / R_L, where E is the induced electromotive force). The induced current passes through the detection coil (e.g., CTI magnetic core), generating a secondary induced current (I). This signal is then processed through multi-stage amplification, filtering, and synchronous demodulation techniques to extract the effective signal. Finally, the resistance is calculated using the formula $R_L = K \times V_{out}/I$ (where K is a calibration coefficient), and the microcontroller (MCU) computes the resistance value, which is then output through the RS485 interface. In addition, to more clearly illustrate the working principle of the equipment used, we show the illustration of the working principle of the equipment and the circuit board in Figure 2. The equivalent circuit of the device is

shown in the figure below. In this circuit, R1 represents the predicted grounding resistance, and R0 is the equivalent resistance of all other tower grounding resistances in parallel, that is:

$$R_0 = R_2 \parallel R_3 \parallel R_4 \parallel \cdots \parallel R_n,$$

where n represents the number of grounding points. As the number of grounding points increases, the value of R0 approaches zero. Therefore, from an engineering perspective, R0 can be approximated as zero. Based on this characteristic, the resistance value measured by the device can be approximated as R1, the target grounding resistance. This device provides highly accurate grounding resistance measurements and is not limited by the traditional grounding resistance measurement methods; therefore, field detection becomes more flexible and efficient. Figure 1(d) shows the working principle and the equivalent circuit of the device.

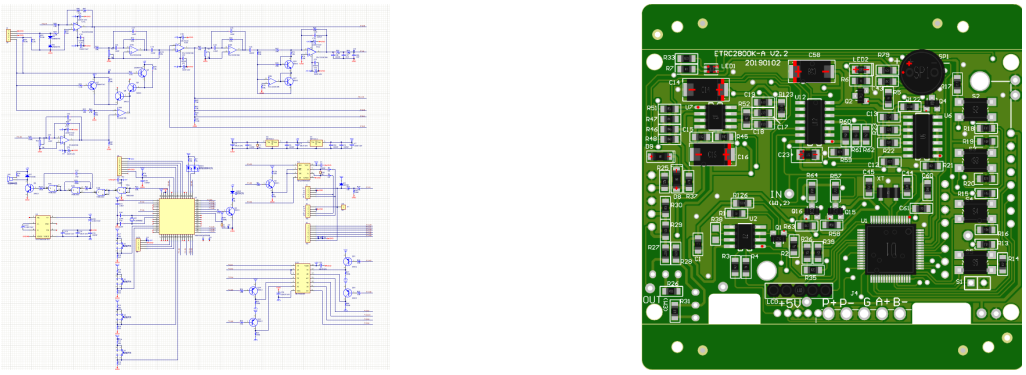

(a) (b)

Figure 2. (a) The schematic diagram of the device's working principle. (b) The circuit board diagram used in the device.

We also monitor the internal temperature of the tower's inclination sensor to indicate the air temperature during the data collection period. The data collection period starts from January 1, 2022 and ends on December 31, 2022. Since we mainly explore the influence of local temperature and humidity on the resistance value of transmission towers in severely cold areas, we collect only data from the low-temperature period in that area. Thus, a total number of 261 pieces of data for both the temperature and grounding resistance time series are adopted for research analysis. In addition, except the factor of the temperature, we also consider that the humidity can affect the values of grounding resistance. Therefore, we collect the precipitation data from https://www.tianqi24.com in Figure 3. From the data in Figure 3, we observe that the precipitation period is mainly concentrated from August to November. Given that the primary influence of precipitation on soil resistivity in this region is the transition between dry and wet states, we hypothesize a threshold effect rather than a linear response to the amount of rainfall. Therefore, to capture this dominant shift in soil moisture, we convert the precipitation data into a binary time series. This is done by designating the high-humidity period (the rainy season) as '1' and all other times as '0', as depicted in Figure 3. This method simplifies the model to focus on the distinct impact of the two major environmental states (dry vs. wet) on grounding resistance.

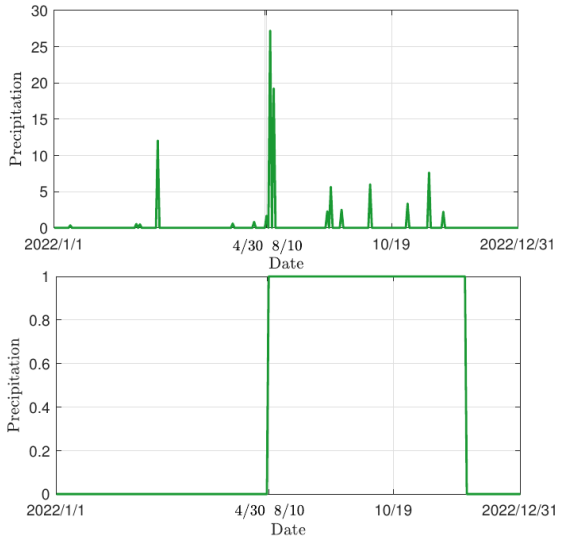

Figure 3. Time series of precipitation data, and precipitation value used for multiple linear regression.

4. Empirical analysis

All computations are executed using MATLAB R2020a on an Intel(R) Core(TM) i5-6200 CPU operating at 2.30 GHz. The specifications of the computer used for the analysis are provided to ensure reproducibility and to offer context regarding the computational resources required for the methods used. While the specifications do not directly influence the outcomes of the data analysis, they may affect processing efficiency, particularly for large datasets or computationally intensive procedures.

We mostly study the correlations between the grounding resistance and the meteorological factors according to the time series data. We first calculate the statistics metrics such as the minimal, maximal, mean, variance, skewness, and kurtosis values for the temperature and the resistance time series. The computed results are listed in Table 1.

Table 1. Descriptive statistics for the temperature and resistance data.

Category	Min	Max	Mean	σ	Skewness	Kurtosis
Temperature ($^{\circ}C$)	-11.0200	28.8600	5.7100	9.7227	0.0638	1.9484
Resistance (Ω)	0.0140	6.0000	2.8225	1.6085	-0.2140	1.6215

Subsequently, we apply a linear regression model to the original temperature and resistance data to calculate the coefficients. In these models, the grounding resistance is treated as the dependent variable, while the raw meteorological factors are the independent variables. Table 2 presents the computed coefficient values along with their corresponding p-values. Notably, the temperature coefficient is statistically important, as its p-value is less than 0.05. Using the coefficients from Table 2, we generate two sets of predicted resistance values. The first, denoted $T_{\text{corrected}}$, is based on the simple linear regression model using only temperature. The second, $TP_{\text{corrected}}$, is based on the multiple linear regression model using both temperature (T_{raw}) and precipitation (P_{raw}). These models are defined

in Eqs (4.1) and (4.2). This enables us to directly compare the predictive power of the two models.

$$T_{\text{corrected}} = \beta_0 + \beta_1 T_{\text{raw}}, \tag{4.1}$$

$$TP_{\text{corrected}} = \tilde{\beta}_0 + \tilde{\beta}_1 T_{\text{raw}} + \beta_2 P_{\text{raw}}, \tag{4.2}$$

where β_0 and $\tilde{\beta}_0$ are the intercept, β_1, $\tilde{\beta}_1$, and β_2 are the coefficient of temperature and precipitation, respectively, shown in Table 2. The regression corrected temperature time series are shown in Figure 4(a). In addition, the regression relationship between the temperature and the resistance is shown in Figure 4(c). The residual distribution under linear regression of temperature and resistance is shown in Figure 4(b). Figure 4(b) shows the residual distribution after performing a linear regression between temperature and resistance. The residuals, plotted against the observations, highlight any unexplained variability by the linear model. A visible pattern in the residuals indicates that the relationship might be more complex than a simple linear model can capture.

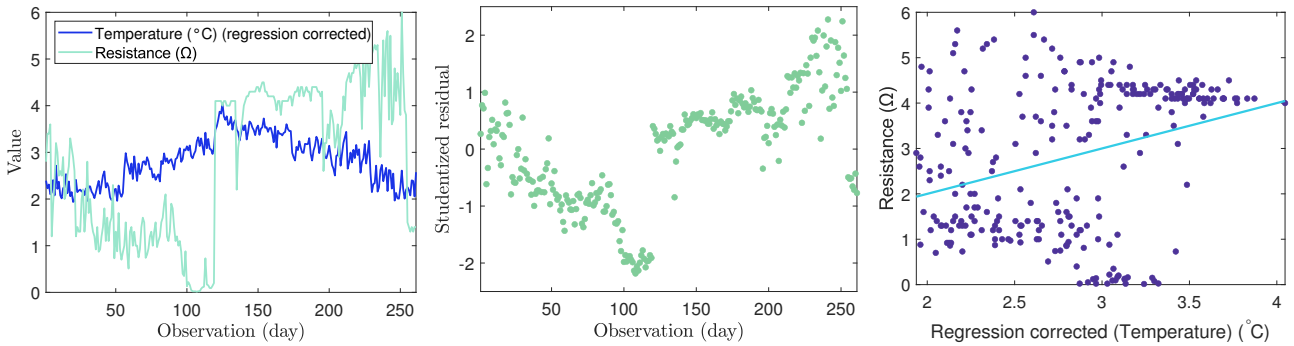

(a) (b) (c)

Figure 4. (a) Trend of temperature time series and resistance, (b) residual distribution under linear regression of temperature (°C) and resistance (Ω), and (c) a comparison of the predicted resistance values from the temperature-only model against the actual measured resistance data.

To better demonstrate the correlation with resistance, we introduce precipitation as an additional independent variable. This enables us to explore the synergistic effect of temperature and precipitation on the grounding resistance value of transmission towers. Using a multiple linear regression model, we calculate the coefficients and corresponding p-values of the dependent variable, resistance, under the independent variables, temperature, and precipitation. Here, all variables are modeled in their physical units: Temperature (°C), resistance (Ω), and precipitation (mm/day; alternatively humidity in %RH). We report unstandardized coefficients so that effects are physically interpretable (e.g., holding the other predictor constant, a 1 °C increase in temperature is associated with a change of β_T Ω in resistance; likewise for precipitation/humidity with β_P Ω per unit). We also diagnose multicollinearity. The results of the coefficients and p-values of the linear regression model are shown in Table 2. According to Figure 5 (a), the resistance fluctuations show a certain temporal alignment with the regression-corrected temperature and precipitation data and according to Figure 5, the residual distribution indicates that the linear model does not fully capture the relationship, suggesting a potential nonlinearity. The residual plot in Figure 5(c) illustrates that grounding resistance is affected by temperature and precipitation. Our analysis indicates that the p-value of the temperature coefficient is lower in the multiple regression

model compared to the single regression model, suggesting greater reliability. Furthermore, the p-value of precipitation coefficient is also below 0.05, confirming its statistical significance.

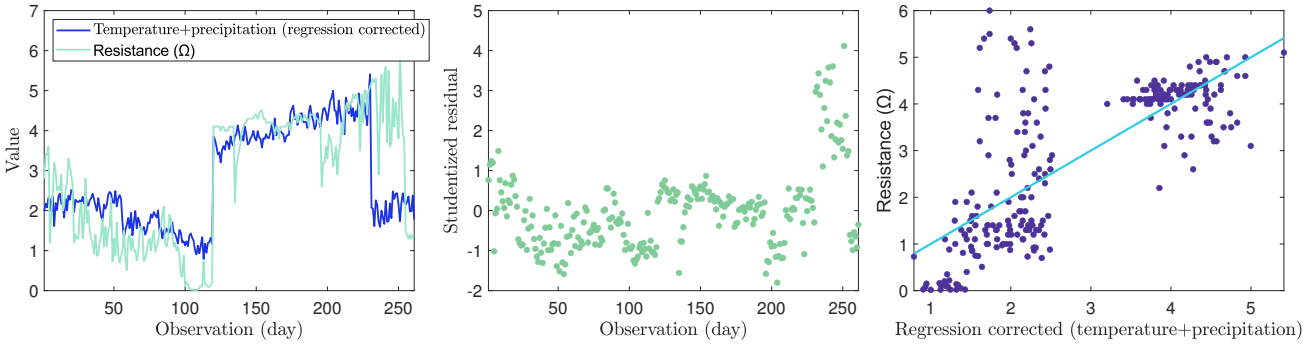

(a) (b) (c)

Figure 5. (a) Trend of temperature time series and resistance, (b) residual distribution under linear regression of temperature (°C) and resistance (Ω), and (c) a comparison of the predicted resistance values from the temperature and precipitation model against the actual measured resistance data.

Table 2. Coefficients and the p-value of multiple linear regression model.

Statistics	Coefficient			p-value		
Series pairs for regression	Intercept	x_1	x_2	Intercept	x_1	x_2
Temperature ($°C$)/Resistance (Ω)	2.5204	0.053	/	1.810e-64	1.291e-07	/
Temperature ($°C$)/Precipitation (mm)/Resistance (Ω)	1.838	-0.0615	3.140	9.217e-58	1.360e-09	8.817e-42

Besides, a noteworthy observation from Table 2 is the inversion of the temperature coefficient's sign between the linear and multiple regression models. In the linear regression model, the coefficient is positive (+0.053), whereas it becomes negative (-0.0615) once precipitation is included. This coefficient reversal is not a contradiction but a result of confounding between temperature and other seasonal factors. The multiple regression model reveals the net effect of temperature: When humidity remains constant, an increase in temperature enhances ion mobility in the soil and, consequently, decreases resistance. Therefore, the result from the multiple regression model more accurately reflects the true physical role of temperature.

Additionally, Table 3 provides the statistical regression evaluation metrics, including RMSE, R^2, Adjusted R^2, and the F-statistic. The units of the variables used in these calculations are listed in Table 2 for reference. RMSE is the mean square root of the error between the predicted value and the true value; the smaller the better. R^2 is the coefficient of determination, and the closer R^2 is to 1, the better. Adjusted R^2 offsets the impact of sample size on R^2 and performs better with larger values. F-statistic is used to verify the overall significance level of the model. Enhanced model reliability is reflected by the decreased RMSE and increased values of R^2, Adjusted R^2, and F-statistic in Table 3.

Table 3. Statistical indicators of multiple linear regression model.

Series pairs for regression	RMSE	R^2	Adjusted R^2	F-statistic
Temperature/Resistance	1.53	0.102	0.0988	29.5
Temperature/precipitation/Resistance	1.07	0.56	0.556	164

To quantify and compare the goodness-of-fit of the two regression models, we use Pearson correlation analysis. We calculate the correlation coefficient between the predicted resistance values from each model ($T_{\text{corrected}}$ and $TP_{\text{corrected}}$) and the actual, measured resistance data. This coefficient serves as a direct measure of model performance, and its square corresponds to the coefficient of determination (R^2), which gives an intuitive indication of how effectively each model explains the variance in the resistance data. The results, including the Pearson correlation coefficient and p-value, are presented in Table 4. The absolute value of the Pearson correlation coefficient indicates the strength of the linear relationship, with values closer to 1 representing stronger correlations. A p-value less than 0.05 signifies statistically significant correlations. Based on the data in Table 4, we observe that the improved model, which includes precipitation as an additional factor, exhibits a significantly stronger linear correlation with resistance compared to the model considering only temperature. To examine whether similar characteristics persist during the summer, we perform a linear regression analysis on data from May to August. The resulting correlations between the fitted values and resistance are analyzed using Pearson correlation, and the results are presented in Table 5. The findings are largely consistent with those observed under low-temperature conditions. However, given that we primarily focus on low-temperature scenarios, we will not delve further into the summer conditions.

Table 4. Pearson correlation between the regressed meteorological and resistance data.

Series pair	Pearson correlation	p-value
Predicted (from Temperature) vs. Actual Resistance	0.4495	7.75e-07
Predicted (from Temperature+precipitation) vs. Actual Resistance	0.7015	4.71e-39

Table 5. Pearson correlation between the regressed meteorological data and resistance values during summer.

Series pair	Pearson correlation	p-value
Temperature (regression)/Resistance	0.3197	1.29e-07
Temperature+precipitation (regression)/Resistance	0.7480	1.16e-46

To enhance the robustness and reliability of our experimental results, we use the Bootstrap resampling technique to evaluate the stability of the findings given the limited dataset. We conduct 1,000 bootstrap iterations on the available data to estimate the confidence intervals of key parameters, including the correlation coefficients and regression coefficients. The results, presented in Figure 6, reveal that the confidence intervals are relatively narrow, indicating the statistical reliability of the results. This analysis demonstrates that, despite the constraints of a single series of measurements, the outcomes remain robust under repeated resampling. The use of Bootstrap resampling not only validates the consistency of our findings but also supports their potential applicability to similar scenarios under comparable environmental conditions. This ensures that the conclusions drawn are

reliable and statistically sound, even with a limited dataset.

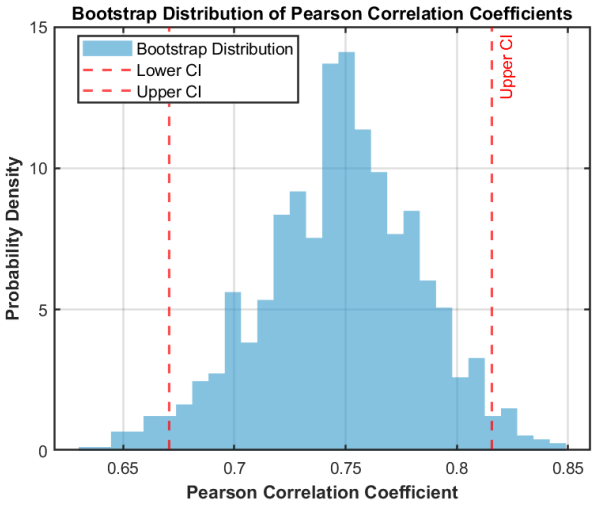

Figure 6. Bootstrap resampling is applied with 1,000 iterations on the dataset to assess the robustness and reliability of the results.

Next, we first take MF-DFA to analyze three types of time series, and multifractal indicators such as the generalized Hurst exponents $H(q)$, scaling exponents $\tau(q)$, and multifractal spectrum are adopted, as shown in Figure 7. The results in Figure 7 imply that temperature, temperature precipitation combination, and resistance time series exhibit multifractal characteristics, and the difference between the maximum and minimum values of Hurst exponents can reflect the strength of multifractal, that is, the stability of the sequence. The results show that the multifractal strength of the resistance sequence is the highest and the least stable. In addition, the intensity of temperature time series is the weakest. The curvature of the scaling exponents $\tau(q)$ curve can also describe the strength of multifractals, and the results indicate the consistency of the above conclusions. Figure 7(c) presents the multifractal spectra, where the width of the spectrum $\Delta\alpha$ quantifies the intensity of multifractality. A larger $\Delta\alpha$ value indicates a stronger multifractal nature and a more complex fluctuation structure within the time series. The analysis demonstrates that the resistance series (blue line) possesses the strongest multifractal properties, as evidenced by its spectrum having the largest width at $\Delta\alpha = 1.2045$. In comparison, the temperature+precipitation series (magenta line) exhibits a moderate degree of multifractality with a spectrum width of $\Delta\alpha = 0.7949$. The temperature-only series (olive line) shows the weakest multifractal characteristics, corresponding to the narrowest spectrum width of $\Delta\alpha = 0.5311$. Furthermore, the $H(2)$ of all the three types of time series are smaller than 0.5, indicating that all the three time series are negative persistence.

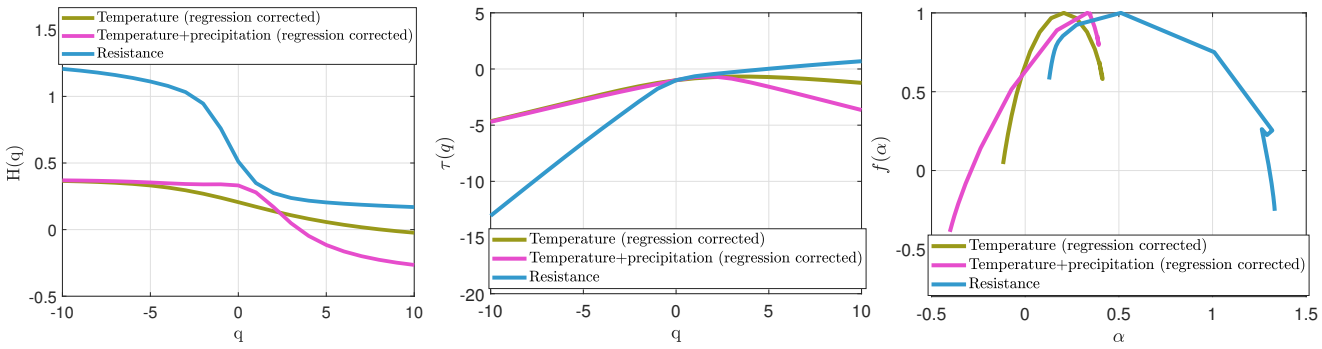

(a) (b) (c)

Figure 7. Multifractal features of three time series under MF-DFA of (a) generalized Hurst exponents, (b) scaling exponents, and (c) multifractal spectrum. A color version of the figure is available in the web version of the article.

To assess the multifractality of the resistance values, we conduct a one-off robustness check on key parameters and report the associated uncertainty intervals. Without altering the main workflow, we vary the detrending order $m \in \{1, 2\}$, the scale ranges $s \in [10, 25], [15, 35], [20, 40]$, and the q-ranges (from $[-5, 5]$ to $[-10, 10]$), as summarized in Figure 8 (a). We then apply a sliding-window ensemble (window length $L = 180$, step $= 15$) to the series (Figure 8 (b)). For each configuration, we compute the distributions of $H(2)$ and the spectrum width $\Delta\alpha$ and summarize them by the mean and 95% confidence intervals (CIs), with stability assessed by the coefficient of variation (CV), shown in Figure 8 (c). The windowed estimates give a mean $H(2) = 0.33$ with 95% CI $[0.30, 0.37]$ and $\Delta\alpha = 1.17$ with 95% CI $[0.84, 1.28]$. Across the parameter grid, the stability metrics are CV$[H(2)] = 0.067$ and CV$[\Delta\alpha] = 0.482$, indicating that while short sample length widens the intervals for $\Delta\alpha$, the directional findings remain unchanged, and the major conclusions are statistically robust and interpretable.

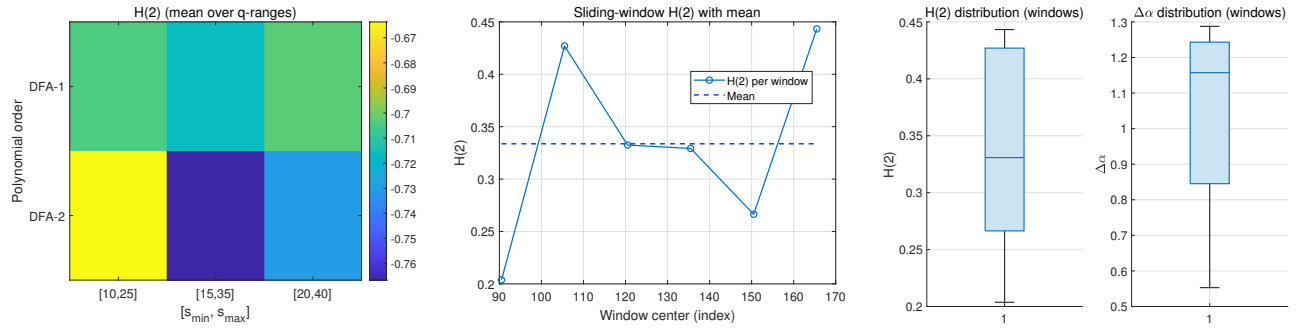

(a) (b) (c)

Figure 8. MF-DFA robustness on the univariate series (here: Resistance). (a) Parameter–sensitivity map of $H(2)$: Columns show scale ranges s, rows show detrending orders m; colors denote $H(2)$ averaged over three q-ranges. (b) Sliding-window estimates of $H(2)$ (window length L=180, step = 15) with mean ± SE band. (c) Window-wise boxplots of $H(2)$ and the spectrum width $\Delta\alpha$. Together, the panels indicate consistent estimates across admissible settings and a stable multifractal structure of the series.

After checking that all three types of sequences have multifractal characteristics, we adopt the MF-DCCA to study the cross-correlation between meteorological factors and resistance. The results of the generalized Hurst exponents, scaling exponents, and multifractal spectrum of the cross-correlation are shown in Figure 9. The results manifest that the ΔH_{xy}, curvature of τ_{xy}, and $\Delta\alpha_{xy}$ of Temperature+precipitation/Resistance are all greater than those of Temperature/Resistance, indicating that the multifractal cross-correlation of Temperature+precipitation/Resistance is stronger. The multifractal spectrum width for Temperature+precipitation/Resistance is $\Delta\alpha_{xy} = 0.9926$, which is larger than the 0.8891 for Temperature/Resistance. Besides, the multifractal cross-correlation persistence of both types of sequence combinations are reflected as positive persistence.

The MF-DCCA results provide deeper insights into the complex, scale-dependent relationship between meteorological factors and grounding resistance, moving beyond simple linear correlations. The stronger multifractal cross-correlation observed for the 'Temperature+Precipitation/Resistance' pair, evidenced by a larger spectrum width ($\Delta\alpha_{xy}$), indicates that the combined effect of temperature and precipitation introduces a richer, more complex fluctuation structure in their relationship with resistance across time scales. The positive persistence ($H_{xy}(2) > 0.5$) found in this cross-correlation suggests that periods of synergistic increase (or decrease) in the combined meteorological factors are likely to be followed by sustained increases (or decreases) in grounding resistance. Physically, this implies that the non-linear interplay between soil moisture (from precipitation) and ion mobility (from temperature) creates a persistent, memory-driven system. For example, a prolonged period of cold and dry weather not only increases resistance in the short term but also establishes a trend that is likely to persist; a dynamic behavior that linear models fail to capture but is effectively characterized by MF-DCCA.

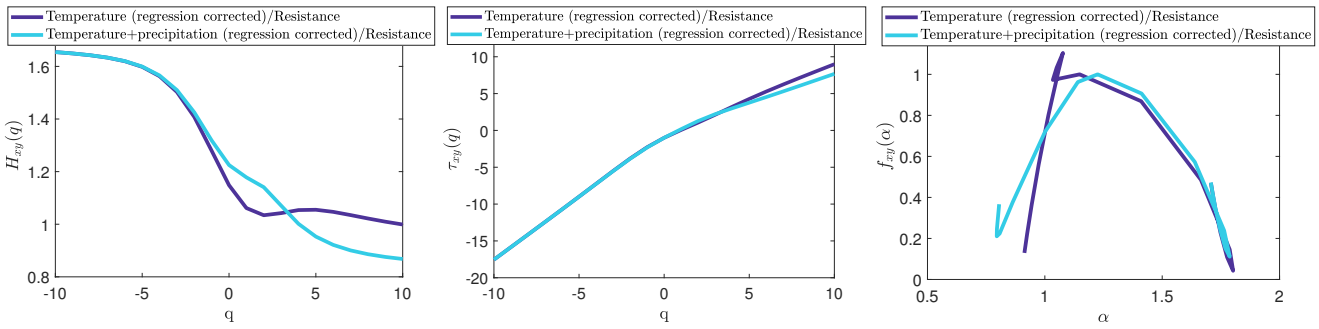

(a) (b) (c)

Figure 9. Multifractal features between any two sequences under MF-DCCA of (a) generalized Hurst exponents, (b) scaling exponents, and (c) multifractal spectrum. A color version of the figure is available in the web version of the article.

To mitigate uncertainty induced by the limited sample size, we perform a one-off robustness check of key MF-DCCA parameters for the temperature+precipitation–resistance relationship and report the associated uncertainty intervals. Without altering the main workflow, we vary the detrending order $m \in \{1, 2\}$, the scale ranges $s \in [10, 25], [15, 35], [20, 40]$, averaged over plausible q-ranges, and apply a sliding-window ensemble (window length $L = 180$, step $= 15$). Figure 10(a) shows the parameter-sweep heatmap of the spectrum width $\Delta\alpha_{xy}$; across all (m, s) combinations, $\Delta\alpha_{xy}$ remains large (roughly 1 to > 2), indicating a robust multifractal cross-correlation

between temperature+precipitation and resistance. Figure 10(b) displays the time-resolved estimates of $H_{xy}(2)$; the windowed mean is around 1.4 with a relatively narrow standard-error band, supporting consistent persistence over time. Figure 10(c) presents the distributions (boxplots) of $H_{xy}(2)$ and $\Delta\alpha_{xy}$ across windows; medians and IQRs are stable, and occasional outliers do not alter the overall conclusions. Taken together, Figures 10(a)–(c) demonstrate that the cross-correlation between temperature+precipitation and resistance exhibits a pronounced and robust multifractal structure with positive persistence, and that the limited sample length mainly broadens the interval of $\Delta\alpha_{xy}$ without changing these directional findings.

It is crucial to acknowledge that these analyses are based on a limited data length (N=261). While our robustness checks (Figures 8 and 10) confirm the stability of the findings, the precision of multifractal exponents from short series is inherently constrained.

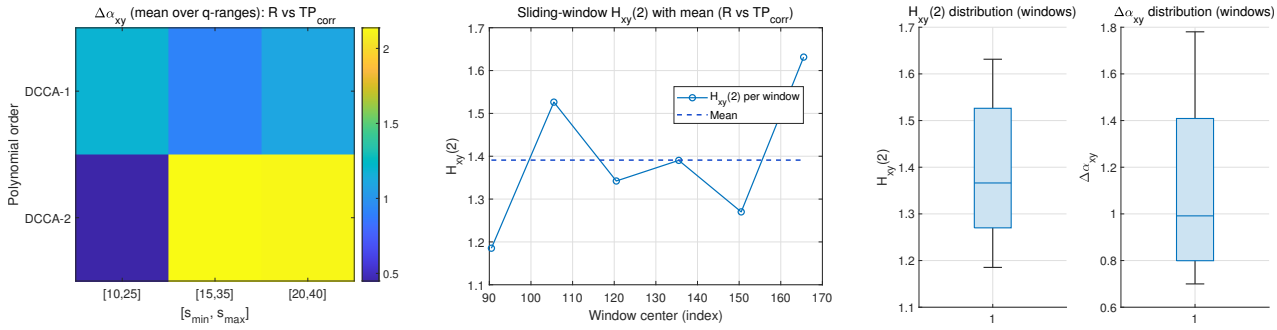

(a) (b) (c)

Figure 10. MF-DCCA robustness and window analysis: (a) Parameter-sensitivity heat map with scales s on the x-axis and detrending order m on the y-axis; color encodes the spectrum width $\Delta\alpha_{xy}$ for R versus T_{corr}+P_{corr}. (b) Sliding-window $H_{xy}(2)$ (window length L=180, step 15) with mean ± SE band. (c) Distributions (box plots) of windowed $H_{xy}(2)$ and $\Delta\alpha_{xy}$. Across admissible settings, results remain stable: T_{corr}+P_{corr}/R shows stronger multifractal cross-correlation, a wider spectrum, and overall positive persistence.

5. Conclusions

In this study, we systematically examined the impact of climatic factors, temperature and precipitation, on the grounding resistance of transmission line towers in extremely cold regions. Our time series analysis revealed that resistance alone exhibits stronger multifractality and anti-persistent behavior compared to meteorological variables. Linear modeling results showed limited correlation between resistance and temperature, while the inclusion of precipitation significantly improved correlation strength and model robustness. Using MF-DFA and MF-DCCA, we confirmed that the resistance data exhibited complex temporal dynamics, and the combination of temperature and precipitation provided stronger multifractal cross-correlations. These findings emphasized the importance of considering nonlinear and multiscale interactions when evaluating grounding systems in cold climates.

It should be emphasized that the contribution of this study is not the proposal of an algorithm, but rather the application of established multifractal analysis to uncover the complex, dynamic coupling between grounding resistance and meteorological factors. This diagnostic approach offers unique

advantages in revealing the system's "memory effects" and non-linear complexity, which are beyond the scope of traditional linear models. Moreover, a primary limitation of this study is the relatively short time series, which restricts the scaling range for multifractal analysis. Although our comprehensive robustness checks support the major conclusions, future research would greatly benefit from longer-term monitoring data. This would enhance the precision and generalizability of our findings, providing a more definitive characterization of the complex relationship between meteorological factors and grounding resistance. Furthermore, building upon the deeper understanding of the system's dynamics gained here, future work will shift toward developing predictive models. We plan to extend this analysis to additional tower locations to evaluate geographical generalizability. Furthermore, we will compare various state-of-the-art (SOTA) predictive methods, such as machine learning algorithms like Long Short-Term Memory (LSTM) networks, and incorporate soil resistivity, freezing depth, and snow cover data to develop more accurate predictive models and early-warning systems, ensuring the resilience and reliability of power infrastructure under extreme climate conditions.

Author contributions

Guangxin Zhang: Conceptualization, methodology, software, writing-original draft; Minzhen Wang: Data curation, validation, visualization; Jian Wang: Formal analysis, investigation; Junseok Kim: Conceptualization, supervision, writing-review & editing. All authors have read and agreed to the published version of the manuscript.

Use of Generative-AI tools declaration

The authors declare they have not used Artificial Intelligence (AI) tools in the creation of this article.

Conflict of interests

The authors declare that there is no conflict of interests regarding the publication of this article.

References

1. V. P. Androvitsaneas, G. J. Tsekouras, I. F. Gonos, I. A. Stathopulos, *Seasonal variation and timeless evolution of ground resistance*, In: 2018 IEEE International Conference on High Voltage Engineering and Application (ICHVE), Athens, Greece, 2018, 1–4. http://dx.doi.org/10.1109/ICHVE.2018.8641909
2. M. Li, Y. Gao, T. Zhang, H. Wu, X. Lao, Z. Chen, *Analysis of soil resistivity characteristics under meteorological conditions in Haikou City*, In: 2017 IEEE 5th International Symposium on Electromagnetic Compatibility (EMC-Beijing), Beijing, China, 2017, 1–5. http://dx.doi.org/10.1109/EMC-B.2017.8260388
3. B. M. Kouchaki, M. L. B. Barry, C. M. Wood, T. Moody, A laboratory investigation of factors influencing the electrical resistivity of different soil types, *Geotech. Test. J.*, **42** (2019), 829–853. http://dx.doi.org/10.1520/GTJ20170364

4. D. M. S. Gerscovich, C. Vipulanandan, Data analyses to correlate the soil properties to the electrical resistivity, *Geotech. Geol. Eng.*, **41** (2023), 4507–4528. http://dx.doi.org/10.1007/s10706-023-02529-y
5. S. Bhatt, P. K. Jain, Correlation between electrical resistivity and water content of sand–a statistical approach, *Am. Int. J. Res. Sci. Technol. Eng. Math.*, **6** (2014), 115–121.
6. M. Kizhlo, A. Kanbergs, *Correlation analysis between grounding resistance and seasonal variations of upper soil resistivity of two-year period in Balozhi, Latvia*, In: International Symposium on Power Electronics Power Electronics, Electrical Drives, Automation and Motion, Sorrento, Italy, 2012, 890–893. http://dx.doi.org/10.1109/SPEEDAM.2012.6264517
7. A. Madikizela, M. Kabeya, I. E. Davidson, *Seasonal variation of soil resistivity and corrective factor for optimal substation earth grid design in Eastern Cape*, In: 2022 30th Southern African Universities Power Engineering Conference (SAUPEC), Durban, South Africa, 2022, 1–6. http://dx.doi.org/10.1109/SAUPEC55179.2022.9730743
8. V. L. Coelho, A. Piantini, H. A. D. Almaguer, R. A. Coelho, W. D. C. Boaventura, J. O. S. Paulino, The influence of seasonal soil moisture on the behavior of soil resistivity and power distribution grounding systems, *Electr. Pow. Syst. Res.*, **118** (2015), 76–82. http://dx.doi.org/10.1016/j.epsr.2014.07.027
9. F. E. Asimakopoulou, G. J. Tsekouras, I. F. Gonos, I. A. Stathopulos, Estimation of seasonal variation of ground resistance using artificial neural networks, *Electr. Pow. Syst. Res.*, **94** (2013), 113–121. http://dx.doi.org/10.1016/j.epsr.2012.07.018
10. A. Rani, N. Kumar, J. Kumar, N. K. Sinha, *Machine learning for soil moisture assessment*, In: Deep learning for sustainable agriculture, Academic Press, 2022, 143–168. http://dx.doi.org/10.1016/B978-0-323-85214-2.00001-X
11. W. D. A. Mahemmdi, A. S. A. Banna, F. H. A. Menshed, The relation between the variation of electrical resistivity values and moisture of soil at Baghdad University, Iraq, *Iraqi J. Sci.*, **64** (2023), 2946–2958. http://dx.doi.org/10.24996/ijs.2023.64.6.23
12. G. Yuan, A. Che, H. Tang, Evaluation of soil damage degree under freeze–thaw cycles through electrical measurements, *Eng. Geol.*, **293** (2021), 106297. http://dx.doi.org/10.1016/j.enggeo.2021.106297
13. J. W. Kantelhardt, S. A. Zschiegner, E. K. Bunde, S. Havlin, A. Bunde, H. E. Stanley, Multifractal detrended fluctuation analysis of nonstationary time series, *Physica A*, **316** (2002), 87–114. http://dx.doi.org/10.1016/S0378-4371(02)01383-3
14. M. Wang, Y. Wang, R. Xu, R. Peng, J. Wang, J. Kim, Multifractal detrended fluctuation analysis combined with Allen–Cahn equation for image segmentation, *Fractal Fract.*, **9** (2025), 310. http://dx.doi.org/10.3390/fractalfract9050310
15. B. Podobnik, H. E. Stanley, Detrended cross-correlation analysis: A new method for analyzing two nonstationary time series, *Phys. Rev. Lett.*, **100** (2008), 084102. https://doi.org/10.1103/PhysRevLett.100.084102
16. N. Xu, S. Li, X. Hui, Multifractal analysis of COVID-19's impact on China's stock market, *Fractals*, **29** (2021), 2150213. https://doi.org/10.1142/S0218348X21502133
17. F. H. A. D. Araujo, L. H. S. Fernandes, Multifractal detrended fluctuations analysis for ibovespa assets, *Fractals*, **29** (2021), 2150183. https://doi.org/10.1142/S0218348X21501838

18. A. Sankaran, T. Plocoste, A. N. G. R. Nair, M. G. Mohan, Unravelling the fractal complexity of temperature datasets across Indian mainland, *Fractal Fract.*, **8** (2024), 241. https://doi.org/10.3390/fractalfract8040241
19. S. J. Duanzhu, J. Wang, C. R. Jia, Hotel comment emotion classification based on the MF-DFA and partial differential equation classifier, *Fractal Fract.*, **7** (2023), 744. https://doi.org/10.3390/fractalfract7100744
20. A. Alam, D. Nikolopoulos, D. Cantzos, M. Tahir, T. Iqbal, E. Petraki, et al., Regional multifractal variability of the overall seismic activity in Pakistan from 1820 to 2020 via the application of MDFA on earthquake catalogs, *Fractal Fract.*, **7** (2023), 857. https://doi.org/10.3390/fractalfract7120857
21. F. Rahmani, M. H. Fattahi, A multifractal cross-correlation investigation into sensitivity and dependence of meteorological and hydrological droughts on precipitation and temperature, *Nat. Hazards*, **109** (2021), 2197–2219. https://doi.org/10.1007/s11069-021-04916-1
22. S. T. Ogunjo, I. Fuwape, A. B. Rabiu, S. S. Oluyamo, Multifractal analysis of air and soil temperatures, *Chaos*, **31** (2021), 033103. https://doi.org/10.1063/5.0029658
23. J. Wang, H. Xu, W. Jiang, Z. Han, J. Kim, A novel MF-DFA-phase-field hybrid MRIs classification system, *Expert Syst. Appl.*, **225** (2023), 120071. https://doi.org/10.1016/j.eswa.2023.120071
24. C. Lee, S. Ham, Y. Hwang, S. Kwak, J. Kim, An explicit fourth-order accurate compact method for the Allen-Cahn equation, *AIMS Math.*, **9** (2024), 735–762. https://doi.org/10.3934/math.2024038
25. J. Wang, M. Huang, X. Wu, J. Kim, A local fitting based multifractal detrend fluctuation analysis method, *Physica A*, **611** (2023), 128476. https://doi.org/10.1016/j.physa.2023.128476
26. R. Zhang, C. Jia, J. Wang, MF-DCCA analysis of investor sentiment and financial market based on NLP algorithm, *J. Korean Soc. Ind. App.*, **28** (2024), 71–87. https://doi.org/10.12941/jksiam.2024.28.071
27. P. Oswiecimka, S. Drozdz, M. Forczek, S. Jadach, J. Kwapien, Detrended cross-correlation analysis consistently extended to multifractality, *Phys. Rev. E*, **89** (2014), 023305. https://doi.org/10.1103/PhysRevE.89.023305
28. Q. Meng, F. Wang, L. Zhao, Incremental policy iteration for unknown nonlinear systems with stability and performance guarantees, *arXiv Preprint*, 2025. https://doi.org/10.48550/arXiv.2508.21367
29. R. T. Q. Chen, Y. Rubanova, J. Bettencourt, D. K. Duvenaud, Neural ordinary differential equations, *Adv. Neural Inf. Process. Syst.*, **31** (2018).
30. A. D. Ames, S. Coogan, M. Egerstedt, G. Notomista, K. Sreenath, P. Tabuada, *Control barrier functions: Theory and applications*, In: 2019 18th European Control Conference (ECC), Naples, Italy, 2019, 3420–3431. https://doi.org/10.23919/ECC.2019.8796030

AIMS Press